

## Research Article

# Effects of Different Penetration Patterns on a Fault during Underground Fluid Injection

Xiaochen Wei,<sup>1,2</sup> Qi Li ,<sup>2,3</sup> Xiaying Li,<sup>2,3</sup> Zhiyong Niu,<sup>2,3</sup> Xiangjun Liu ,<sup>4</sup> and Lixi Liang<sup>4</sup>

<sup>1</sup>School of Geoscience and Technology, Southwest Petroleum University, Chengdu 610500, China

<sup>2</sup>State Key Laboratory of Geomechanics and Geotechnical Engineering, Institute of Rock and Soil Mechanics, Chinese Academy of Sciences, Wuhan 430071, China

<sup>3</sup>University of Chinese Academy of Sciences, Beijing 100049, China

<sup>4</sup>State Key Laboratory of Oil and Gas Reservoir Geology and Exploitation, Southwest Petroleum University, Chengdu 610500, China

Correspondence should be addressed to Qi Li; [qli@whrsm.ac.cn](mailto:qli@whrsm.ac.cn)

Received 4 September 2018; Revised 3 December 2018; Accepted 24 December 2018; Published 8 April 2019

Guest Editor: Victor Vilarrasa

Copyright © 2019 Xiaochen Wei et al. This is an open access article distributed under the Creative Commons Attribution License, which permits unrestricted use, distribution, and reproduction in any medium, provided the original work is properly cited.

At underground fluid injection sites with natural faults, understanding how to avoid the subsequent fault reactivation and induced seismicity plays a crucial role in the success of subsurface anthropogenic activities. In this work, with the objective of avoiding risky faults in site selection in the Shengli Oilfield, we investigated the faults that are usually encountered in the target demonstration zone; based on the geophysical observations of fault structures, we designed different fault tectonic scenarios to investigate the different penetration patterns of faults. We used the finite element-based numerical method to assess the influence of the effective lateral and vertical reservoir transmissivity in each fault penetration pattern. Our results indicate that when a permeable fault intersects into the target reservoir, it presents both barrier effect to reservoir transmissivity within the target reservoir and hydraulic connection between reservoirs. The effective lateral reservoir transmissivity is dominated by the barrier effect of the fault, and the effective vertical reservoir transmissivity is dominated by the hydraulic connection between reservoirs. Relatively impermeable faults with less contact with the target aquifer make higher effective lateral reservoir transmissivity and lower effective vertical reservoir transmissivity, which would mitigate the risk of caprock failure and the magnitude of the induced seismicity.

## 1. Introduction

Over the last four decades, the induced seismicity has been observed to result from a certain number of underground fluid injection activities including hydrothermal- and petrothermal-enhanced geothermal systems [1], water subsurface disposal [2], enhanced oil/gas recovery (EOR/EGR) [3], and carbon capture and storage that enable the capture of CO<sub>2</sub> from industrial processes and storage in depleted oil/gas fields or deep saline formations [4]. A successful commercial scale deployment of underground fluid injection requires assurance that the injected fluid at each potential geological sequestration site is confined [5–8]. The most significant aspect of containment is the seal potential of the reservoir [9], which could be defined as the seal geometry and seal integrity [10–12]. Seal geometry refers to the

thickness and lateral extent of the caprock, as well as fault tectonics. For long-term security of fluid injection in geological reservoir, the caprock must have sufficient lateral extent to cover the reservoir [13, 14]. Faults are complex and heterogeneous geological systems, and reservoir-scale faults in low-permeability deformed reservoir target for underground fluid injection can present highly complex architecture, which might influence the hydromechanical behavior of the fault system [15–17]. Seal integrity refers to the geomechanical properties of the geological sequestration site. These properties are controlled by the mineralogy [18], the regional and local stress fields [19], and stress changes induced by underground fluid injection [20]. The perturbation of the stress field within a geological formation during and after fluid injection may lead to mechanical failures of the caprock and interior faults [21]. Natural faults are inevitable at

CO<sub>2</sub>-EGS sites such as the North-German Basin and Taupo Volcanic Zone in New Zealand [22, 23]. Underground fluid injection reduces the effective normal stress and brings a preexisting fault to failure, which could generate seismicity occasionally large enough to cause damage [24–26]. Another possible risk related to failure is the potential creation of new leakage pathways for the trapped fluid that may eventually induce earthquakes felt at the ground surface [27–30]. Fundamentally, a well-characterized site must shed light on at least two features of the subsurface: the caprock confining the reservoirs and any faults or fractures crosscutting the formation [31–34]. When caprock is crosscut by faults, its vertical sealing potential will be affected in certain degrees [35]. This critical situation is well illustrated by what happened at some actual sequestration sites (e.g., Weyburn, Canada) [36]. An important question is then related to the issue of faults crosscutting the caprock and the reservoir, i.e., different spatial distributions of a fixed-length fault, which might influence the stress distribution and eventually influence the fault stability during fluid injection [37, 38].

Previous studies on the fault tectonics have indicated the importance of the fault zone architecture to the seal integrity [39–41] and the fault behavior [42–44]. Concerns have been raised related to the complex tectonics in the reservoirs and the surrounding faults, as well as the physical and chemical processes impacting fluid migrations and containment under field conditions [45–47]. The potential for geomechanical failure caused by underground fluid injection has been investigated [15, 16, 48, 49]. Regarding the issue of fault architecture, the first investigations revealed that the spatial distribution of the fault might influence the stress distribution and eventually the fault stability during fluid injection [50–53]. An evolution of the damage zone’s properties with distance from the fault core has been assumed by Rohmer et al. [17], and a geostatistical approach based on observations of fault structures at Navacelles (France) was used to investigate fault stability during injection [54]. Zoback and Gorelick [4] claimed that carbon geological sequestration in deep saline formations is very likely to trigger induced seismicity capable of damaging the caprock, which could ruin the objective of keeping fluid stored deep underground. However, Vilarrasa and Carrera [30] recently argued that induced earthquakes that are large enough to be felt due to geologic carbon geological sequestration are unlikely because sedimentary formations, which are softer than the crystalline basement, are rarely critically stressed. In addition, they argue that fluid leakage through fault reactivation is unlikely because the high clay content of caprock ensures a reduced permeability and increased entry pressure along localized deformation zones. In fact, their standpoints are under the assumption of specific reservoir-caprock sequences and seal geometry, as well as their geomechanical properties and injected fluid behavior under long-term geological sequestration. Thus, it is necessary to have a sufficient knowledge about the tectonics and mechanical properties of formations in the operation site of fluid injection, as well as their long-term influence to ensure that injected fluid would be stored safely over the intended life of the injection project [55, 56].

In this work, with the objective of assessing earthquake risk in the operating region, we investigated the fault slippage with different penetration patterns that are usually encountered in the G89 Block of the CO<sub>2</sub>-EOR demonstration zone in the Shengli Oilfield (Shandong province, China) [57]. The relatively lower permeability than that of the reservoir of the fault has a significant impact on the pressure perturbations within the thick reservoir. When the fault penetrates into different reservoirs, it acts in both the barrier within the target reservoir and hydraulic connection between reservoirs. Focusing on the effective lateral reservoir transmissivity and effective vertical reservoir transmissivity under three penetration patterns caused by different fault tectonic scenarios, we introduce numerical model-coupled changes of pore pressure and stresses. In Section 2, the geomechanical models are described in detail for different scenarios of a fault penetrating into regional caprock, as well as their geomechanical properties. In Section 3, the influence of effective lateral reservoir transmissivity is thoroughly evaluated on pore pressure change, vertical displacement, and the fault slippage and a sensitivity analysis of hydraulic connection is carried out. Finally, the main findings and conclusions are summarized in Section 4.

## 2. Model and Methodology

### 2.1. Theoretical Background

**2.1.1. Frictional Slip on Fault.** An extended version of the classical isotropic Coulomb friction model is provided with all contact analysis capabilities. The extensions include an additional limit on the allowable shear stress and isotropic friction coefficient.

The standard Coulomb friction model assumes that no relative motion occurs if the equivalent frictional stress  $\tau_{eq} = \sqrt{\tau_1^2 + \tau_2^2}$  is less than the critical stress  $\tau_{crit}$ , which is proportional to the contact pressure  $p$ , in the form  $\tau_{crit} = \mu p$ , where  $\mu$  is the friction coefficient that can be defined as a function of the contact pressure  $p$ , the slip rate  $\gamma_{eq}$ , the average surface temperature at the contact point, and the average field variables at the contact point.

Here, it is possible to put an additional limit on the critical stress:  $\tau_{crit} = \min(\mu p, \tau_{max})$ ; if the equivalent stress is at the critical stress  $\tau_{eq} = \tau_{crit}$ , slip can occur. If the friction is isotropic, the direction of the slip and the frictional stress coincide, which is expressed in the form

$$\frac{\tau_i}{\tau_{eq}} = \frac{\gamma_i}{\gamma_{eq}}, \quad (1)$$

where  $\gamma_i$  is the slip rate in direction  $i$  and  $\gamma_{eq}$  is the magnitude of the slip velocity.

$$\gamma_{eq} = \sqrt{\gamma_1^2 + \gamma_2^2}. \quad (2)$$

According to the relationship presented by Hanks [58], the quantification of the overall size of an earthquake is generally based on the seismic moment ( $M_0$ ) which is defined by

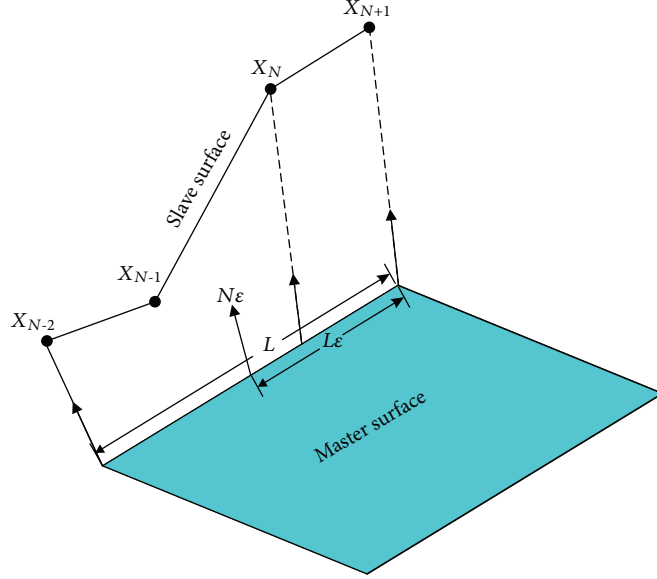


FIGURE 1: Slave nodes interacting with a two-dimensional master surface.

$M_0 = GA d_{avg}$ , and we can approach the seismic moment from the average fault slippage ( $d_{avg}$ ) over the ruptured area (A) and the rock shear modulus (G). In terms of seismic moment, the magnitude ( $M$ ) of an earthquake is given by  $M_w = 2(\log_{10}(M_0) - 9.1)/3$  [59]. Therefore, to some extent, in this study, the average fault slippage ( $d_{avg}$ ) determines the magnitude of the seismic event induced by the simulated fluid injection.

**2.1.2. The Master-Slave Contact Algorithm.** Herein, a master-slave contact algorithm is adopted for governing the interaction behavior between a fault and the surrounding rock. Figure 1 illustrates a typical master-slave slide line segment. Before initiating the search for the nodal subset of the master surface nodes that will interact with each node on the slave surface, the unit normal vectors are computed for all of the nodes on the master surface. Additional unit normal vectors are computed for each segment at a distance  $\epsilon L$  from the end of each segment, where  $\epsilon$  is a fraction and  $L$  is the length of the segment.

For the two-dimensional small-sliding deformable contact, a point on the contact line associated with a slave node  $X_{N+1}$  is represented by the vector:

$$P(\epsilon) = X_0 + \epsilon v. \quad (3)$$

As described previously, the line's anchor point  $X_0$  and its tangent vector  $v$  are functions of the current master node coordinate. Hence, the vector  $v$  is, in general, a nonunit vector. Linearization of equation (3) yields

$$\delta h n + h \delta n = \delta x_0 + \delta \epsilon v + \epsilon \delta v - \delta u_{N+1}, \quad (4)$$

where  $\delta u_{N+1} = \delta(X_{N+1} + u_{N+1}) = \delta x_{N+1}$ ,  $\delta x_0 = N_i(u_0) \delta x_i$ , and  $\delta v = R \cdot N_i^u(u_0) \delta x_i$ . Taking the dot product of equation (4) with  $n$  results in the following expression for  $\delta h$ :

$$\delta h = -n \cdot (\delta u_{N+1} - \delta x_0 - \delta \epsilon v). \quad (5)$$

Likewise, taking the dot product of equation (4) with the normalized tangent vector  $t = v/|v|$  and setting  $h = 0$  results in the following expression for the variation in slip:

$$\delta s \stackrel{\text{def}}{=} \delta \epsilon v \cdot t = t \cdot (\delta u_{N+1} - \delta x_0 - \epsilon \delta v). \quad (6)$$

Suitable expressions for  $d\delta h$  and  $d\delta s$  can be derived by linearizing equation (4) and applying the techniques highlighted above [60].

**2.2. Conceptual Model.** To investigate the stress changes and fault responses during CO<sub>2</sub> storage, we used a geomechanical model that coupled changes of pore pressure and stresses. The numerical models present typical penetration patterns on faults that are usually encountered in the G89 Block of the target demonstration zone in the Shengli Oilfield at an approximate depth of 1000 m [57]. The target zone is located in the south-west of the Shengli Oilfield, which was estimated to have approximately 40 million tons of initial oil-in-place. The G89 Block is in the middle of the Jinjia-Zhenglizhuang-Fanjia structure, which belongs to the Dongying depression. It covers an area of 4.1 km<sup>2</sup> and is composed of several interbedded producing zones (Figure 2) [35]. The target reservoir is filled with fine quartz sandstone, and fluid injection was proposed for secondary recovery.

**2.3. Model Setup.** In this study, to reflect the real regional structural settings in the demonstration zone, based on their geophysical observations of fault structures in the G89 Block in Figure 2, three typical penetration patterns on a fault are



(a)

Erathem Era	System period	Formation	Depth	Rock formation	Lithologic characteristic	Reservoir caprock	
Cenozoic	Neogene	Guantao	1000	[Yellow layer]	Thin sand-shale interbedded	Reservoir	
			1200				
	Paleogene	Dongying	1400	[Purple layer]	Primarily composed of thick sandstone with a pure mudstone top of approximately 50 m	Reservoir	
			1600				
		Shahejie	1800	[Green layer]	Oil shale	Regional caprock	
			1800		Grey mudstone		
			2000		Primarily composed of thick sandstone		Reservoir
			2000		Mudstone deposits		
			2200		Mudstone deposits in southern work area with thick bodies and a small range		Partial caprock
			2200				
2400	[Blue layer]	Oil shale mudstone	Regional caprock				
2400		Cream mudstone and oil shale					
Kongdian	3000	[Light blue layer]	Thin sand-shale interbedded	Reservoir			

(b)

FIGURE 2: Location of the Sinopec Shengli Oilfield and the strata of the G89 Block of the target demonstration zone in the Shengli Oilfield [35].

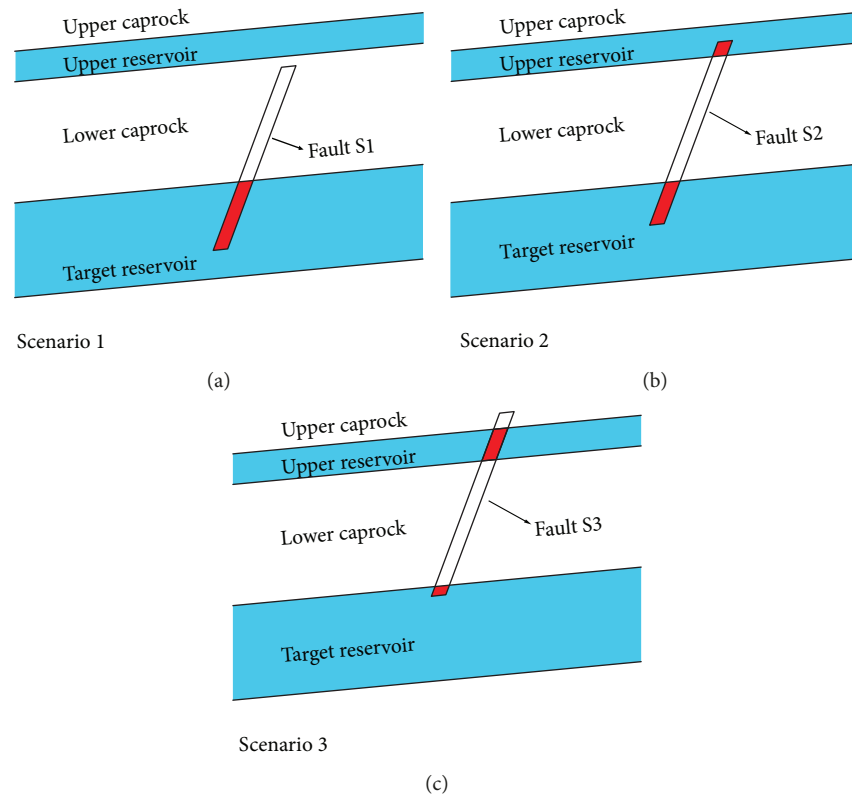


FIGURE 3: Conceptual models for three scenarios investigated in the study.

currently considered (Figure 3). 2-D numerical models are employed to take into account the geomechanical aspects of supercritical  $\text{CO}_2$  injection into the reservoir. To restrict the complexity of our model conceptualization and better identify the individual unit behavior, two assumptions were made: (1) two reservoir-seal associations are used while the lower reservoir is the targeted reservoir. Instead of an aquifer system with numerous complex interbed distribution reality, two reservoir-seal associations allow us to understand such a formation's behavior in a straightforward manner and (2) the hydraulic connection of each fault zone is assumed isotropic. As the constant permeability in the fault zone is considerably lower than that in the aquifer, it is only a trivial extension to include anisotropic permeability [61]. The injected supercritical  $\text{CO}_2$  is defined with a density of  $1.1 \text{ g/cm}^3$  and viscosity of  $0.02 \text{ mPa}\cdot\text{s}$ , and the phase change is neglected in this work.

*Scenario 1.* The fault does not penetrate into the upper reservoir. The lower caprock is above the target reservoir, and the rocks in the lower caprock have not been completely penetrated. There are still intact sections with a certain thickness on the top, and the fault retains a vertical sealing ability. The fluid cannot leak out through such a fault. This pattern is the most developed scenario in the demonstration zone, accounting for 66% of the total number of faults.

*Scenario 2.* The permeable fault penetrates into the upper reservoir but does not reach the upper caprock. In this way, the transverse sealing ability is still strong. The hydraulic connection of the fault under such a scenario is good enough to

allow the leakage of fluid through the fault and diffusion from the target reservoir to the upper reservoir. The Scenario 2 fault in the demonstration zone is relatively developed, accounting for 30% of the total number of faults.

*Scenario 3.* The permeable fault penetrates the two reservoirs into the upper caprock. Due to the hydraulic connection of the fault, the fluid could theoretically leak into the upper reservoir along the fault [35].

Figure 4 shows the geometry and initial conditions of the numerical model ( $1500 \text{ m} \times 10000 \text{ m}$ ) that we used for modeling the three types of fault settings. The model extends from 1000 to 2500 m in depth and horizontally far enough from the injection zone (10000 m) to simulate laterally infinite conditions. The fault zone is located at a distance of 800 m from the injection well, dipping  $60^\circ$ , with a 50 m length along the dip and a 700 m long fault surface. The reservoir is initially saturated by water and the initial pore pressure is assumed to be hydrostatic (shown as  $P_0$  in Figure 4). For each of the tectonic stress regimes, the vertical stress is considered to be given by the weight of the overburden and vertical stress from the weight of overburden rock for a density of  $\rho = 2600 \text{ kg/m}^3$ , with horizontal stress being scaled by a factor 0.6 of the vertical stress, i.e.,  $S_h = 0.6S_v$ . The fluid is injected into the target reservoir at  $-2000 \text{ m}$  for 20 years through a horizontal well, and the injection pressure is stable at 30 MPa, which corresponds to the industrial injection pressure. The rock mechanical properties are based on available logs and well data from the field and laboratory experiments.

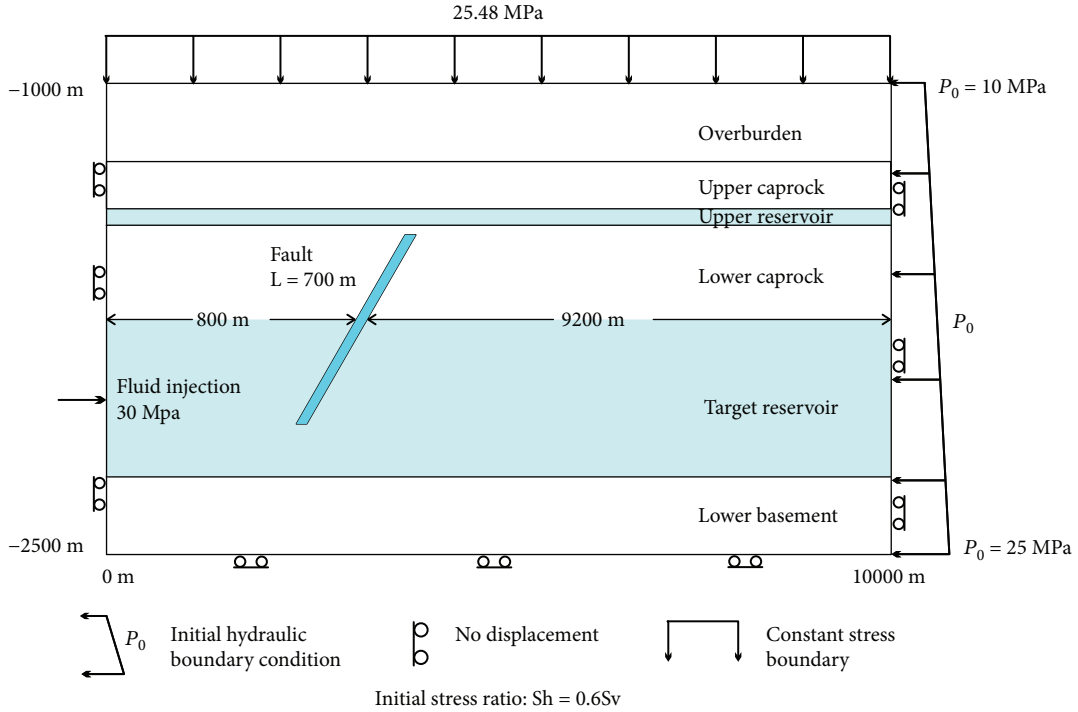


FIGURE 4: Schematic representation of the model geometry and the boundary conditions of Scenario 1. The general numerical model settings of the three scenarios are only different in vertical fault location.

TABLE 1: Material properties.

	Young's modulus (GPa)	Poisson's ratio	Permeability (mD)	Porosity	Density ( $\text{kg/m}^3$ )	Friction angle ( $^\circ$ )	Cohesion (MPa)
Caprock	30	0.37	$1.0 \times 10^{-2}$	0.01	2600	30	9
Reservoir	43	0.30	$1.0 \times 10^5$	0.20	2600	22	15
Fault	10	0.30	$1.0 \times 10^4$	0.10	2600	22	15

Hydraulic and mechanical properties for the different layers (the caprock, reservoir, and fault) are listed in Table 1 (after [53, 62]), and the target reservoir was fractured before  $\text{CO}_2$ -EOR operation.

The schematic views of the model geometry and the corresponding numerical models, as well as the boundary conditions, are presented in Figure 4. The lengths of the faults in each scenario are the same; the only difference is the intersection of fault into formations. The multiple layers and the fault are modeled using an elastoplastic isotropic Mohr-Coulomb model. The normal displacements applied to the lateral boundaries were fixed to zero. The vertical displacement at the bottom of the geomechanical model was also fixed to zero. A calculated initialization was performed to reach a geomechanical equilibrium between the initial geostress fields and the applied boundary conditions of the model. To enhance the computational accuracy and efficiency, a structured mesh with 26902 elements was adopted in the numerical model. The grid around the injection point and faults was densified, and the size of the finest element is  $2.0 \text{ m} \times 2.0 \text{ m}$ .

The pore pressure distribution was presented in Figure 5 after 20 years of injection. In Scenario 1, the fault intersects the target reservoir on a very large surface and so creates a low-permeability barrier in the upper portion of the reservoir, while in Scenario 3, the fault intersects the target reservoir on a relatively smaller surface and Scenario 2 is an intermediate case. In Scenario 2 and Scenario 3, the permeable fault penetrates into the upper reservoir, the injected fluid leaks along the fault and results in a pore pressure rise in the upper reservoir.

### 3. Results and Discussion

**3.1. Pore Pressure Changes.** An increase in the pore pressure results in a general reduction of the mean effective stresses in the reservoir and caprock system. According to the work of Mathias et al. [6], the lithostatic stress varies vertically from the free ground surface and the largest change is occurring in the lower part of the caprock. For this reason, in this study, we focus on the mechanical responses along the interface between the lower caprock and target reservoir from the

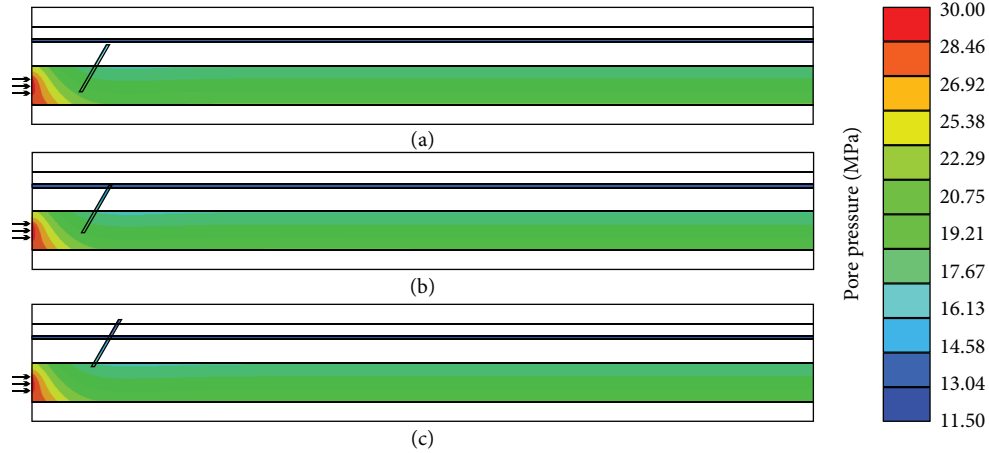


FIGURE 5: The pore pressure distribution of Scenario 1, Scenario 2, and Scenario 3 was presented in (a), (b), and (c), respectively, after 20 years of injection.

injection well to the fault at different times and locations after the start of injection.

Figure 6 presents the pore pressure changes along the interface (shown in insert sketch plots) at different times. As shown, pore pressure changes increase with time at all locations after the injection starts, and at specific times, the maximum increase in pore pressure occurs near the injection well zone and farther locations experience less pore pressure increase. After 20 years of injection, the pore pressure at the crosscutting point of the fault point  $N$  increases to 17.853 MPa, 17.851 MPa, and 17.755 MPa in Scenario 1, Scenario 2, and Scenario 3, respectively. The relatively lower pore pressure at point  $N$  in Scenario 3 indicates the barrier effect of the fault within the target reservoir, which depends on the section of the reservoir thickness that is intersected by the fault. When a fault with relatively lower permeability intersects into the targeted reservoir in a large section such as those in Scenario 1 and Scenario 2, the effective lateral reservoir transmissivity is significantly reduced and the injected fluid accumulates at the fault and generates significant overpressure, while in Scenario 3, the much less contact between the fault and the target reservoir indicates better effective lateral reservoir transmissivity and, consequently, pore pressure would experience less increase.

Other than the barrier effect of the fault within the target reservoir, the hydraulic connection between reservoirs enables the injected fluid to flow upward into the upper reservoir and thus dissipates the overpressure at the fault. As shown in Figure 4, the pore pressure transmits from the target reservoir to the upper reservoir along the fault in Scenario 2 while hydraulic connection is missing in Scenario 1 for the fault does not reach the upper reservoir. For this reason, the relatively lower pore pressure at point  $N$  in Scenario 2 than in Scenario 1 suggests that the hydraulic connection between reservoirs in Scenario 2 mitigate the overpressure at the fault, even in a limited scale.

Figure 7 illustrates the variations of pore pressure versus time at three different locations with horizontal distances (200 m, 400 m, and 600 m) along the interface between the caprock and the reservoir from the injection well for the three

scenarios. As shown, for the locations away from the injection well such as P2 and P3, the pore pressure does not show significant increase after the start of fluid injection in a short time, but after a period of fluid injection, a large volume of the injected fluid leads to an overpressure at all locations in the reservoir and the pore pressure rises towards the initial injection pressure in all scenarios. Pore pressure increases gradually from the hydrostatic pressure 17.50 MPa with time at all three locations. This result is consistent with the work of many different researchers on actual geological sequestration sites [17, 56].

The dashed lines in Figure 7 indicate the time when the pore pressure starts to increase at P1, P2, and P3 in the three scenarios. As shown, the time for the pore pressure to start to rise is dependent on the effective lateral transmissivity of the reservoir. The higher effective lateral transmissivity of the reservoir in Scenario 3 significantly brings forward the time for pore pressure to start to rise than in other scenarios. And at P2 and P3, due to the relatively better effective lateral transmissivity in Scenario 2, the time for pore pressure to start to rise is several days earlier than that in Scenario 1. It can thus be concluded that a higher effective lateral transmissivity of the reservoir brings forward the time for pore pressure to start to rise.

Figure 8 shows that the vertical displacement increases gradually with time during the fluid injection in all three scenarios. Due to the high overpressure near the injection well, the effective stresses change accordingly and thus generate greater vertical displacements near the injection well. As shown, the maximum increase in vertical displacement occurs around the injection well and farther locations experience less of an increase [63]. This result highlights that the higher effective lateral reservoir transmissivity leads to relatively smaller overpressure, which leads to the corresponding smaller scale of vertical displacement.

**3.2. Failure of Caprock.** Caprock failure during underground fluid injection and the corresponding induced seismicity has been studied previously by many different researchers from the perspective of the stress state [64–66]. A higher pore

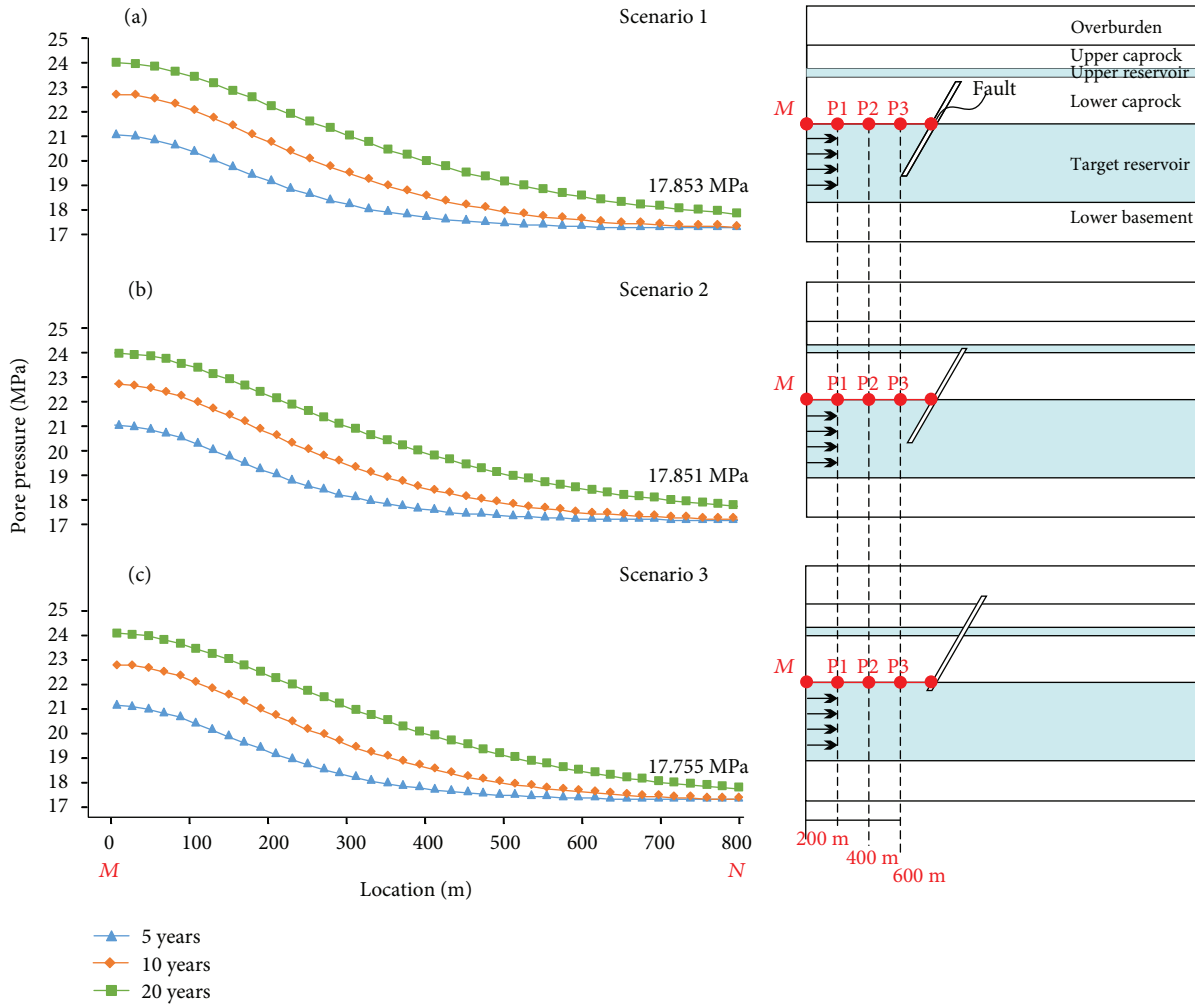


FIGURE 6: Pore pressure distribution along the interface between caprock and reservoir from the injection well to the fault (between point  $M$  and point  $N$ ) at different times. (a), (b), and (c) present the pore pressure distribution on the interface in Scenario 1, Scenario 2, and Scenario 3, respectively.  $N$  is the crosscutting point of the fault, and  $M$  is the crosscutting point of the injection well in all three scenarios. Red dots  $P1$ ,  $P2$ , and  $P3$  locate at 200 m, 400 m, and 600 m, respectively, from the injection well.

pressure rise corresponds to a higher reduction in effective stress; risk of failure rises with time before fluid dissolution [67]. Figure 9 presents the stress state at point  $M$  at the caprock interface near the injection well. As shown, the vertical effective stress decreases with time shortly after the injection starts. After 20 years, the effective stress changes ( $\Delta\sigma'$ ) are 4.476 MPa, 4.472 MPa, and 4.469 MPa in Scenario 1, Scenario 2, and Scenario 3, respectively. In an ideal normal fault stress regime where  $S_v = \sigma_1$  and  $S_h = \sigma_3$ , overpressure can potentially increase the horizontal stresses ( $\sigma_3$ ), while the vertical stress ( $\sigma_1$ ) is likely to remain unaffected, so the diameter of the Mohr circle is reduced as a result of overpressure. Because of the 9 MPa cohesion, the caprock undergoes no failure and remains stable in all three scenarios after 20 years of fluid injection. Due to the higher effective stress changes in Scenario 1, it is more critical compared with those in other scenarios.

**3.3. Fault Slippage.** Despite the tiny differences in pressure and displacement between the three scenarios, the slippage

is very different. Figure 10 shows the fault slippage lengths and pore pressure distributions along the fault surfaces in the three different scenarios. After fluid injection, the original hydrostatic pore pressure distributions show clear variation at the interface of the caprock and the reservoir. Because of the different values of friction angle in the caprock and the fault, the most stressed region in the caprock near the injection well does not fail while the fault fails.

The maximum slippage length value and its location are different in each scenario. In Scenario 1 and Scenario 2, the induced fault slippages reach the maximum values in the target reservoir and decrease with distance into the caprock and present significant change at the interface between the lower caprock and the target reservoir. The reason behind this behavior is in the different material properties, the faults present larger slipping length in the high-permeability reservoir than in the caprock, this tendency is more significant in Scenario 3, the two peak fault slippage values are located in the target reservoir and the

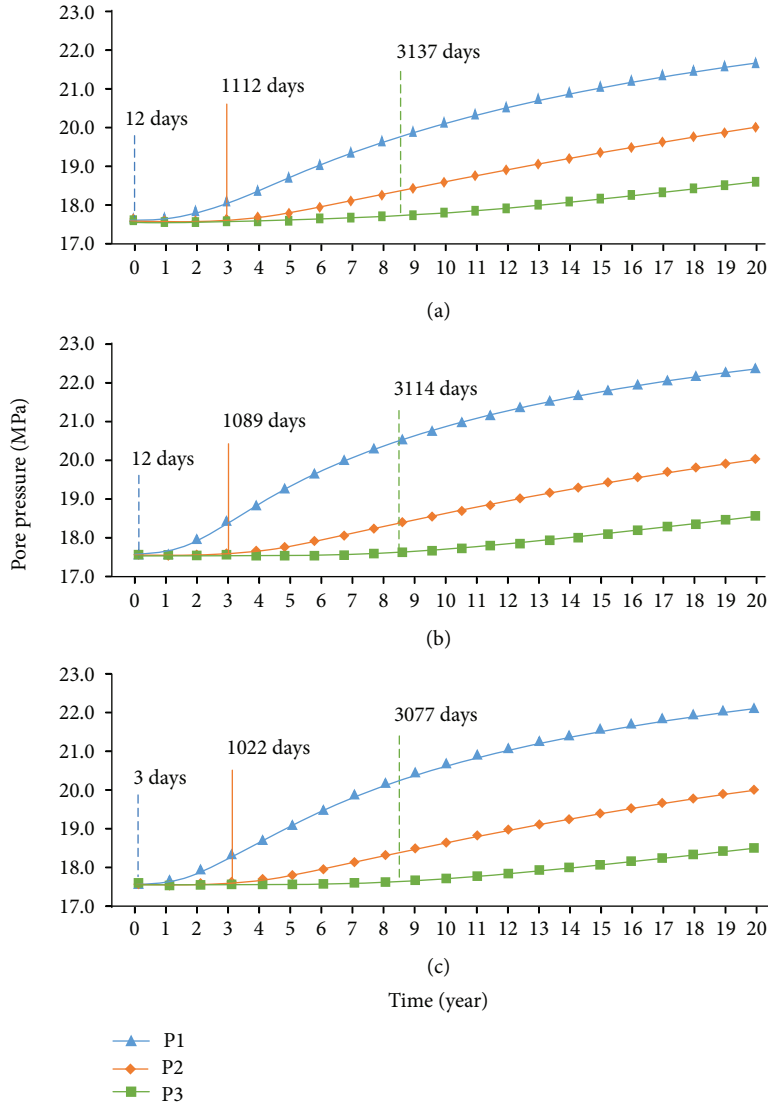


FIGURE 7: Pore pressure versus time at P1, P2, and P3 (shown in Figure 6) along the interface between lower caprock and target reservoir in three scenarios. Dashed lines indicate the time for pore pressure to start to rise at P1, P2, and P3 in all three scenarios.

upper reservoir, and this result is in consistency with the research of Cappa and Rutqvist [68].

As discussed above, the effective lateral reservoir transmissivity, which controls the overpressure at the fault, is significantly affected by the barrier effect of the fault. The effective vertical reservoir transmissivity is controlled by hydraulic connection between reservoirs; the average fault slippages in Scenario 2 (2.735 mm) and Scenario 3 (2.022 mm) are greater than in Scenario 1 (1.944 mm) and so does the maximum fault slippage. The magnitude of fault slippage is affected by both the effective lateral reservoir transmissivity and the effective vertical reservoir transmissivity. The effective vertical reservoir transmissivity dominates the magnitude of fault slippage; when hydraulic connection is missing in Scenario 1, the induced fault slippage remains low; on the other hand, lower effective lateral reservoir transmissivity could generate

significant overpressure along the fault; for this reason, the level of fault slippage in Scenario 2 is greater than that in Scenario 3.

Moreover, the activation of a similar shear slip within the caprock or within the reservoir has very different effects. Even though the faults present larger slipping length in the reservoir than in the caprock, the higher shear modulus  $G$  in the caprock would also enlarge the seismic moment. From these simulation results and the relationships presented in Section 2.1.2, we can calculate the magnitude ( $M$ ) of an earthquake from  $M_0 = \sum G_i A d_i$  and  $M_w = 2(\log_{10}(M_0) - 9.1)/3$ . With an assumed lateral extent of 1 km for rupture since our simulations are conducted in a plane strain model, the magnitudes of 1.58, 1.53, and 1.24 are estimated for the seismic events induced by the simulated fluid injection in Scenario 1, Scenario 2, and Scenario 3, respectively.

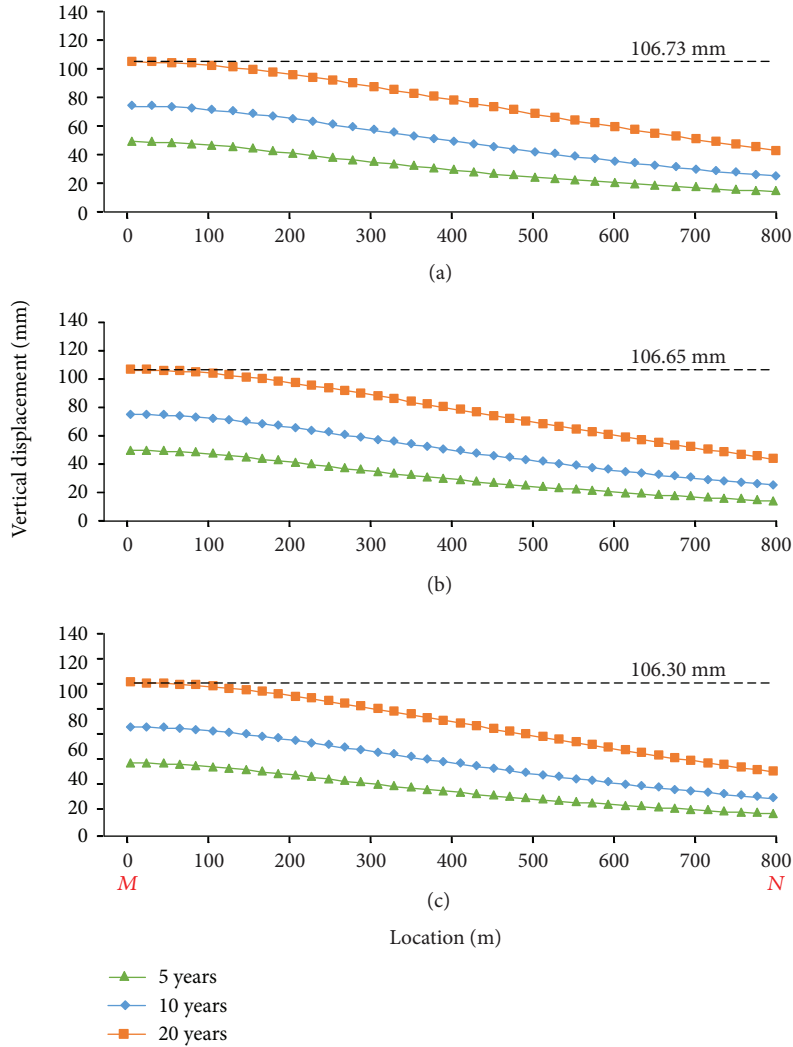


FIGURE 8: Vertical displacement distribution along the interface between lower caprock and targeted reservoir from the injection well to the fault at different locations. (a), (b), and (c) present the vertical displacement distribution in Scenario 1, Scenario 2, and Scenario 3, respectively, on the interface (between point  $M$  and point  $N$  in Figure 6). Black dashed lines show the vertical displacement at point  $M$  after the fluid injection of 20 years.

**3.4. Sensitivity Analysis of Hydraulic Connection.** In the previous section, the presented fault slippage is found to be largely dependent on the effective vertical reservoir transmissivity, which is determined by the hydraulic connection between reservoirs. In this section, we present a sensitivity analysis to clarify the influence of hydraulic connection on the simulation results.

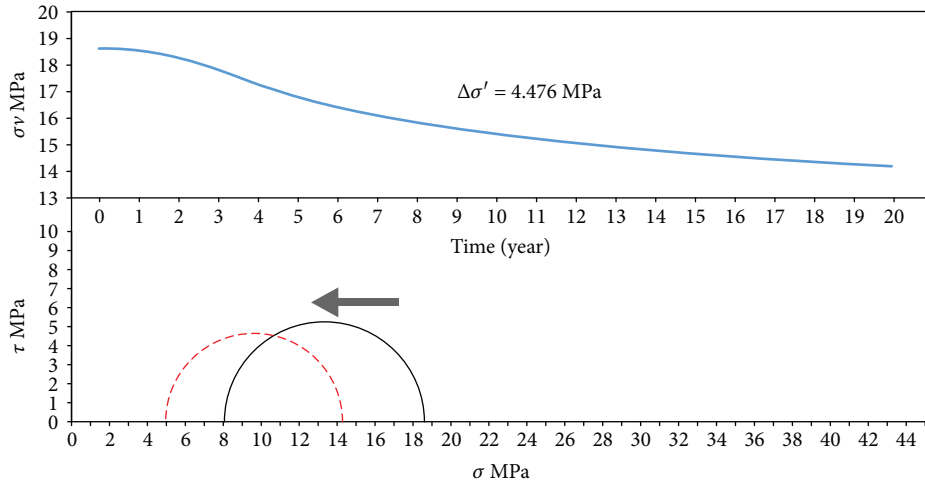
Figure 11 shows that the reduced effective vertical reservoir transmissivity enhances the overpressure along the fault surface within the target reservoir. When the fault permeability decreases to  $K_3 = 1.0 \times 10^3$  mD, the corresponding average fault slippage is 2.622 mm. In contrast, the enlarged fault permeability  $K_1 = 1.0 \times 10^5$  mD enhances the vertical reservoir transmissivity accordingly; as a consequence, the pore pressure shows no obvious change but the corresponding average fault slippage reaches maximum in this sensitivity study at 2.764 mm. This result highlights that both the average fault slippage and maximum fault slippage are dominated by the effective vertical reservoir

transmissivity; when a fault connects two reservoirs, a higher fault permeability would enlarge the fault slippage and the magnitude of the corresponding induced seismicity.

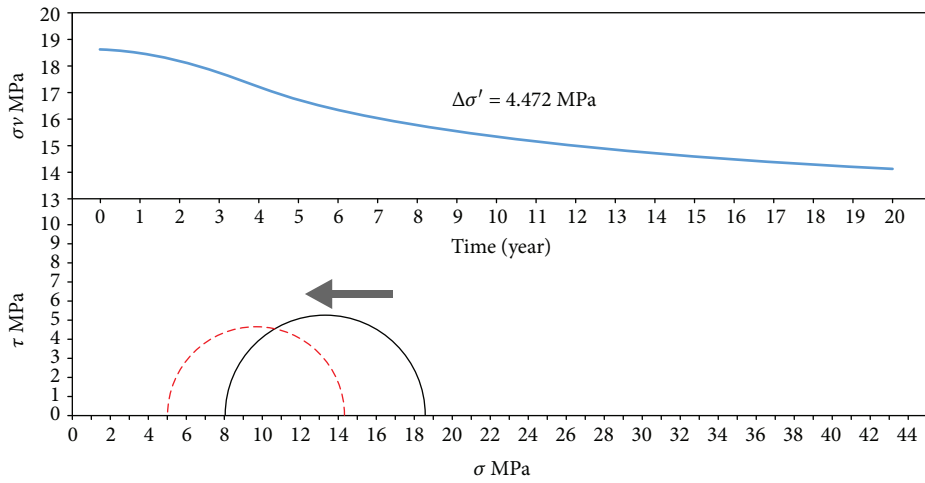
## 4. Conclusions

With the objective of avoiding risky faults in site selection in the Shengli Oilfield, we investigated the faults that are usually encountered in the target demonstration zone. Based on their geophysical observations of fault structures, we designed different fault tectonic scenarios to investigate the different penetration patterns of faults. We implemented a coupled flow and stress model to investigate the influence of the effective lateral and vertical reservoir transmissivity in three different scenarios. We thereby reached the following conclusions:

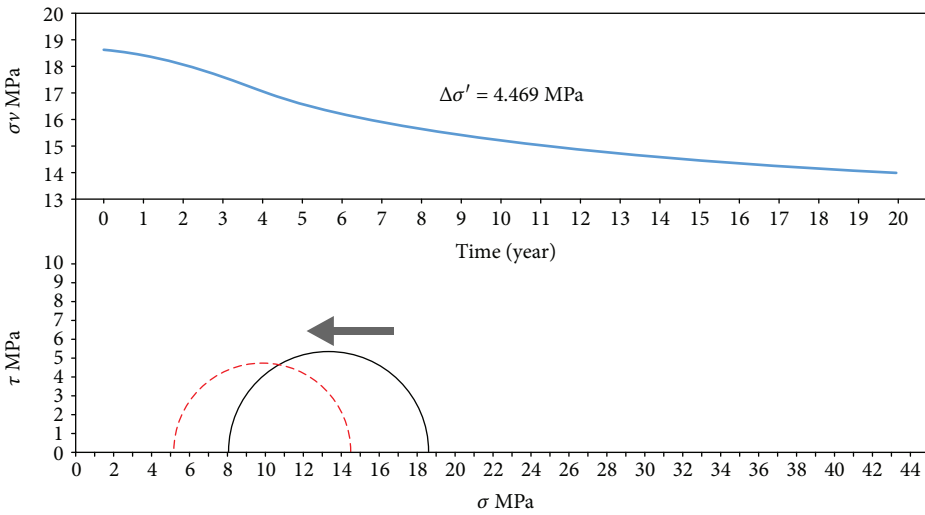
- (1) When a permeable fault intersects into the target reservoir, to reservoir transmissivity, it presents both barrier effect within the target reservoir and



(a)



(b)



(c)

FIGURE 9: Changes on the effective stress state at point *M* (shown in Figure 6). (a), (b), and (c) display the effective stress versus time at point *M* for Scenario 1, Scenario 2, and Scenario 3, respectively.  $\sigma_v$  refers to the vertical effective stress. The solid Mohr's circle represents the initial stress state at point *M*, and red dashed Mohr's circle represents the stress state after 20 years.

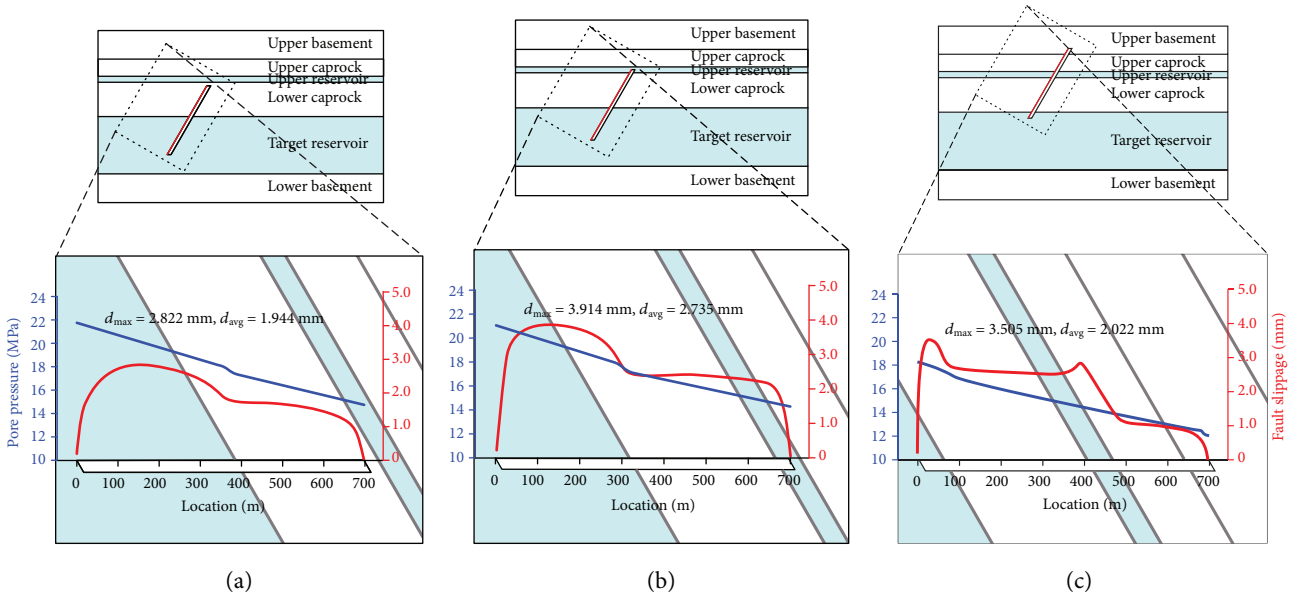


FIGURE 10: Fault slippage lengths (red lines) and pore pressure distributions (blue lines) along the fault surfaces in three scenarios. (a), (b), and (c) display rotation views of faults in Scenario 1, Scenario 2, and Scenario 3, respectively.  $d_{max}$  represents the maximum fault slippage while  $d_{avg}$  represents the average fault slippage.

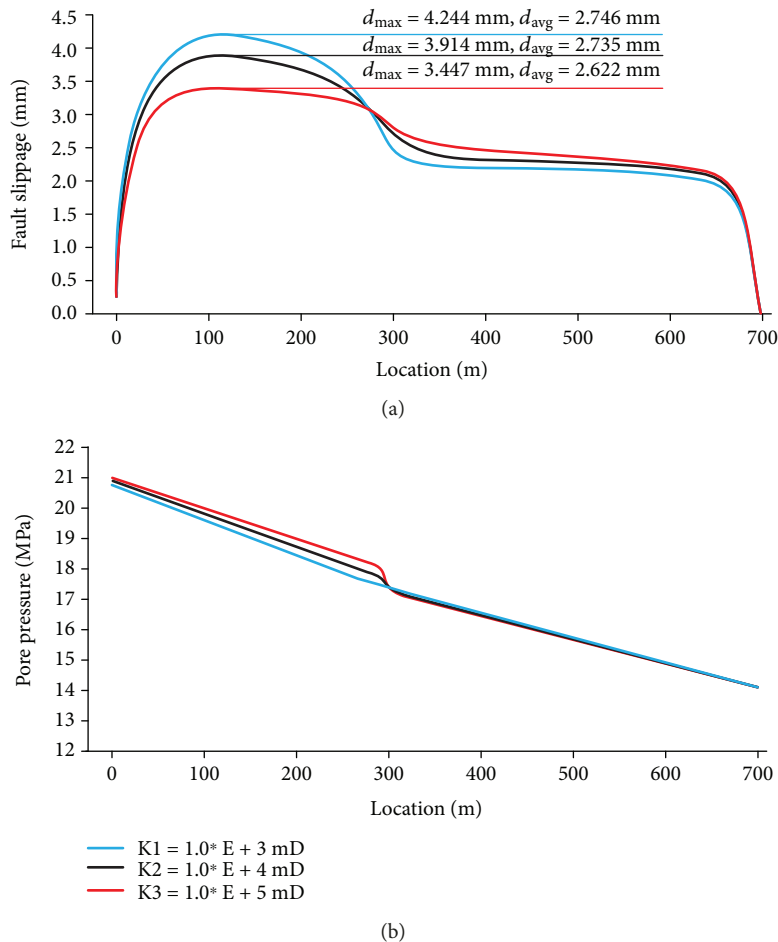


FIGURE 11: Fault slippage lengths and pore pressure distributions along the fault surface in Scenario 2 for different fault permeabilities.

hydraulic connection between reservoirs. The effective lateral reservoir transmissivity is dominated by the barrier effect of the fault, which depends on the section of the aquifer thickness that is intersected by the fault. The effective vertical reservoir transmissivity is dominated by the hydraulic connection between reservoirs, while the hydraulic connection enhances the effective lateral reservoir transmissivity only in a limited scale

- (2) A higher effective lateral reservoir transmissivity could effectively reduce the overpressure in the aquifer and the corresponding scale of vertical displacement, as well as bring forward the time for pore pressure to start to rise at the locations away from the injection well
- (3) Although the caprock undergoes no failure and remains stable in all three scenarios after 20 years of fluid injection, risk of failure rises with time and the most critical state occurs at the end of injection. Compared with those in Scenario 2 and Scenario 3, the situation in Scenario 1 is more critical for higher effective stress change caused by lower effective lateral reservoir transmissivity
- (4) The induced fault slippage reaches the maximum value in the target reservoir and decreases with distance into the caprock. The effective vertical reservoir transmissivity dominates the magnitude of fault slippage, and better hydraulic connection between reservoirs could enlarge the fault slippage and the magnitude of the corresponding induced seismicity

Finally, in underground fluid injection operation such as hydrothermal- and petrothermal-enhanced geothermal systems with hidden faults in the target zone, relatively impermeable faults with less contact with the target aquifer make higher effective lateral reservoir transmissivity and lower effective vertical reservoir transmissivity. Based on the above conclusions, this fault penetration pattern with less contact to the target aquifer would mitigate the risk of caprock failure and the magnitude of the induced seismicity.

### Data Availability

The experiment data used to support the findings of this study are available from the corresponding author upon request.

### Conflicts of Interest

The authors declare that they have no conflicts of interest.

### Acknowledgments

This work was mainly supported by the National Natural Science Foundation of China (NSFC) under Grant no. 41872210, the Open Research Fund of the State Key Laboratory of Geomechanics and Geotechnical Engineering under Grant no. Z017008, and the Young Scholars Development

Fund of SWPU under Grant no. 201699010097. We would also like to thank the financial support provided by the China National Key Technology R&D Program (Grant no. 2012BAC24B05), the United Fund Project of the National Natural Science Foundation of China (Grant no. U1262209), and the National Science and Technology Major Project of the Ministry of Science and Technology of China "Development of Large Oil and Gas Field and Coalbed Methane" (Grant no. 2016ZX05044-004-001).

### References

- [1] E. L. Majer and J. E. Peterson, "The impact of injection on seismicity at The Geysers, California Geothermal Field," *International Journal of Rock Mechanics and Mining Sciences*, vol. 44, no. 8, pp. 1079–1090, 2007.
- [2] A. Mcgarr, "Maximum magnitude earthquakes induced by fluid injection," *Journal of Geophysical Research: Solid Earth*, vol. 119, no. 2, pp. 1008–1019, 2014.
- [3] J. L. Rubinstein and A. B. Mahani, "Myths and facts on wastewater injection, hydraulic fracturing, enhanced oil recovery, and induced seismicity," *Seismological Research Letters*, vol. 86, no. 4, pp. 1060–1067, 2015.
- [4] M. D. Zoback and S. M. Gorelick, "Earthquake triggering and large-scale geologic storage of carbon dioxide," *Proceedings of the National Academy of Sciences of the United States of America*, vol. 109, no. 26, pp. 10164–10168, 2012.
- [5] Q. Li, Y.-N. Wei, G. Liu, and H. Shi, "CO<sub>2</sub>-EWR: a cleaner solution for coal chemical industry in China," *Journal of Cleaner Production*, vol. 103, pp. 330–337, 2015.
- [6] S. A. Mathias, P. E. Hardisty, M. R. Trudell, and R. W. Zimmerman, "Screening and selection of sites for CO<sub>2</sub> sequestration based on pressure buildup," *International Journal of Greenhouse Gas Control*, vol. 3, no. 5, pp. 577–585, 2009.
- [7] T. Reinsch, P. Dobson, H. Asanuma, E. Huenges, F. Poletto, and B. Sanjuan, "Utilizing supercritical geothermal systems: a review of past ventures and ongoing research activities," *Geothermal Energy*, vol. 5, no. 1, p. 16, 2017.
- [8] D. X. Yang, R. S. Zeng, Y. Zhang, Z. Q. Wang, S. Wang, and C. Jin, "Numerical simulation of multiphase flows of CO<sub>2</sub> storage in saline aquifers in Daqingzijing Oilfield, China," *Clean Technologies and Environmental Policy*, vol. 14, no. 4, pp. 609–618, 2012.
- [9] B. Bai, G. Lü, X. Li, Z. Li, Y. Wang, and Q. Hu, "Quantitative measures for characterizing the sealing ability of caprock with pore networks in CO<sub>2</sub> geological storage," *Energy Procedia*, vol. 63, pp. 5435–5442, 2014.
- [10] K. L. Johnson, *Contact Mechanics*, Cambridge University Press, Cambridge, UK, 1987.
- [11] C. H. Juang, C. Carranza-Torres, G. Crosta et al., "Engineering geology — a fifty year perspective," *Engineering Geology*, vol. 201, pp. 67–70, 2016.
- [12] E. Konstantinovskaya, M. Malo, and D. A. Castillo, "Present-day stress analysis of the St. Lawrence Lowlands sedimentary basin (Canada) and implications for caprock integrity during CO<sub>2</sub> injection operations," *Tectonophysics*, vol. 518–521, pp. 119–137, 2012.
- [13] S. De Simone, V. Vilarrasa, J. Carrera, A. Alcolea, and P. Meier, "Thermal coupling may control mechanical stability of geothermal reservoirs during cold water injection," *Physics and*

- Chemistry of the Earth, Parts A/B/C*, vol. 64, pp. 117–126, 2013.
- [14] A. M. H. Plummakers and A. R. Niemeijer, “Healing and sliding stability of simulated anhydrite fault gouge: effects of water, temperature and CO<sub>2</sub>,” *Tectonophysics*, vol. 656, pp. 111–130, 2015.
- [15] P. Jeanne, Y. Guglielmi, F. Cappa, A. P. Rinaldi, and J. Rutqvist, “The effects of lateral property variations on fault-zone reactivation by fluid pressurization: application to CO<sub>2</sub> pressurization effects within major and undetected fault zones,” *Journal of Structural Geology*, vol. 62, pp. 97–108, 2014.
- [16] A. P. Rinaldi, P. Jeanne, J. Rutqvist, F. Cappa, and Y. Guglielmi, “Effects of fault-zone architecture on earthquake magnitude and gas leakage related to CO<sub>2</sub> injection in a multi-layered sedimentary system,” *Greenhouse Gases: Science and Technology*, vol. 4, no. 1, pp. 99–120, 2014.
- [17] J. Rohmer, C. Allanic, B. Bourguine et al., “Improving our knowledge on the hydro-chemo-mechanical behaviour of fault zones in the context of CO<sub>2</sub> geological storage,” *Energy Procedia*, vol. 63, pp. 3371–3378, 2014.
- [18] V. Roche, C. Homberg, and M. Rocher, “Architecture and growth of normal fault zones in multilayer systems: a 3D field analysis in the South-Eastern Basin, France,” *Journal of Structural Geology*, vol. 37, pp. 19–35, 2012.
- [19] P. Segall and S. D. Fitzgerald, “A note on induced stress changes in hydrocarbon and geothermal reservoirs,” *Tectonophysics*, vol. 289, no. 1–3, pp. 117–128, 1998.
- [20] P. Martínez-Garzón, M. Bohnhoff, G. Kwiatek, and G. Dresen, “Stress tensor changes related to fluid injection at the Geysers geothermal field, California,” *Geophysical Research Letters*, vol. 40, no. 11, pp. 2596–2601, 2013.
- [21] J. Rutqvist, A. P. Rinaldi, F. Cappa et al., “Fault activation and induced seismicity in geological carbon storage—lessons learned from recent modeling studies,” *Journal of Rock Mechanics and Geotechnical Engineering*, vol. 8, no. 6, pp. 789–804, 2016.
- [22] M. Alber and C. Solibida, “Geomechanical characterization of a host rock for enhanced geothermal system in the North-German Basin,” *Procedia Engineering*, vol. 191, pp. 158–163, 2017.
- [23] D. D. McNamara, C. Massiot, and S. M. Milichich, “Characterizing the subsurface structure and stress of New Zealand’s geothermal fields using borehole images,” *Energy Procedia*, vol. 125, pp. 273–282, 2017.
- [24] S. Gheibi, R. M. Holt, and V. Vilarrasa, “Stress path evolution during fluid injection into geological formations,” in *50th U.S. Rock Mechanics/Geomechanics Symposium*, pp. 1–13, Houston, TX, USA, 2016, American Rock Mechanics Association.
- [25] Y. Guglielmi, F. Cappa, J. P. Avouac, P. Henry, and D. Elsworth, “Seismicity triggered by fluid injection—induced aseismic slip,” *Science*, vol. 348, no. 6240, pp. 1224–1226, 2015.
- [26] V. Vilarrasa and J. Rutqvist, “Thermal effects on geologic carbon storage,” *Earth-Science Reviews*, vol. 165, pp. 245–256, 2017.
- [27] S. Bigi, S. E. Beaubien, G. Ciotoli et al., “Mantle-derived CO<sub>2</sub> migration along active faults within an extensional basin margin (Fiumicino, Rome, Italy),” *Tectonophysics*, vol. 637, pp. 137–149, 2014.
- [28] M. Lindenfeld, G. Rumpker, K. Link, D. Koehn, and A. Batte, “Fluid-triggered earthquake swarms in the Rwenzori region, East African Rift—evidence for rift initiation,” *Tectonophysics*, vol. 566–567, pp. 95–104, 2012.
- [29] J. Rutqvist, F. Cappa, A. P. Rinaldi, and M. Godano, “Modeling of induced seismicity and ground vibrations associated with geologic CO<sub>2</sub> storage, and assessing their effects on surface structures and human perception,” *International Journal of Greenhouse Gas Control*, vol. 24, pp. 64–77, 2014.
- [30] V. Vilarrasa and J. Carrera, “Geologic carbon storage is unlikely to trigger large earthquakes and reactivate faults through which CO<sub>2</sub> could leak,” *Proceedings of the National Academy of Sciences of the United States of America*, vol. 112, no. 19, pp. 5938–5943, 2015.
- [31] J. W. Johnson, J. J. Nitao, and J. P. Morris, “Reactive transport modeling of cap-rock integrity during natural and engineered CO<sub>2</sub> storage,” in *Carbon Dioxide Capture for Storage in Deep Geologic Formations*, pp. 787–813, Elsevier, 2005.
- [32] J. Rutqvist and C.-F. Tsang, “A study of caprock hydromechanical changes associated with CO<sub>2</sub>-injection into a brine formation,” *Environmental Geology*, vol. 42, no. 2–3, pp. 296–305, 2002.
- [33] R. Shukla, P. Ranjith, A. Haque, and X. Choi, “A review of studies on CO<sub>2</sub> sequestration and caprock integrity,” *Fuel*, vol. 89, no. 10, pp. 2651–2664, 2010.
- [34] R. Shukla, P. G. Ranjith, S. K. Choi, A. Haque, M. Yellishetty, and L. Hong, “Mechanical behaviour of reservoir rock under brine saturation,” *Rock Mechanics and Rock Engineering*, vol. 46, no. 1, pp. 83–93, 2013.
- [35] G. Lv, Q. Li, S. Wang, and X. Li, “Key techniques of reservoir engineering and injection—production process for CO<sub>2</sub> flooding in China’s SINOPEC Shengli Oilfield,” *Journal of CO<sub>2</sub> Utilization*, vol. 11, pp. 31–40, 2015.
- [36] J. P. Verdon, J.-M. Kendall, D. J. White, and D. A. Angus, “Linking microseismic event observations with geomechanical models to minimise the risks of storing CO<sub>2</sub> in geological formations,” *Earth and Planetary Science Letters*, vol. 305, no. 1–2, pp. 143–152, 2011.
- [37] S. Gheibi, R. M. Holt, and V. Vilarrasa, “Effect of faults on stress path evolution during reservoir pressurization,” *International Journal of Greenhouse Gas Control*, vol. 63, pp. 412–430, 2017.
- [38] S. Hirano and T. Yamashita, “Analysis of the static stress field around faults lying along and intersecting a bimaterial interface,” *Geophysical Journal International*, vol. 187, no. 3, pp. 1460–1478, 2011.
- [39] A. Aydin, “Small faults formed as deformation bands in sandstone,” *Pure and Applied Geophysics*, vol. 116, no. 4–5, pp. 913–930, 1978.
- [40] P. Jeanne, Y. Guglielmi, J. Lamarche, F. Cappa, and L. Marié, “Architectural characteristics and petrophysical properties evolution of a strike-slip fault zone in a fractured porous carbonate reservoir,” *Journal of Structural Geology*, vol. 44, pp. 93–109, 2012.
- [41] E. Tondi, M. Antonellini, A. Aydin, L. Marchegiani, and G. Cello, “The role of deformation bands, stylolites and sheared stylolites in fault development in carbonate grainstones of Majella Mountain, Italy,” *Journal of Structural Geology*, vol. 28, no. 3, pp. 376–391, 2006.
- [42] F. Magri, M. Cacace, T. Fischer, O. Kolditz, W. Wang, and N. Watanabe, “Thermal convection of viscous fluids in a faulted system: 3D benchmark for numerical codes,” *Energy Procedia*, vol. 125, pp. 310–317, 2017.

- [43] L. C. Pereira, L. J. N. Guimarães, B. Horowitz, and M. Sánchez, "Coupled hydro-mechanical fault reactivation analysis incorporating evidence theory for uncertainty quantification," *Computers and Geotechnics*, vol. 56, pp. 202–215, 2014.
- [44] V. Vilarrasa, R. Makhnenko, and S. Gheibi, "Geomechanical analysis of the influence of CO<sub>2</sub> injection location on fault stability," *Journal of Rock Mechanics and Geotechnical Engineering*, vol. 8, no. 6, pp. 805–818, 2016.
- [45] J. Lee, K.-B. Min, and J. Rutqvist, "Probabilistic analysis of fracture reactivation associated with deep underground CO<sub>2</sub> injection," *Rock Mechanics and Rock Engineering*, vol. 46, no. 4, pp. 801–820, 2013.
- [46] X. Lei, S. Ma, W. Chen, C. Pang, J. Zeng, and B. Jiang, "A detailed view of the injection-induced seismicity in a natural gas reservoir in Zigong, southwestern Sichuan Basin, China," *Journal of Geophysical Research: Solid Earth*, vol. 118, no. 8, pp. 4296–4311, 2013.
- [47] H. Xing, Y. Liu, J. Gao, and S. Chen, "Recent development in numerical simulation of enhanced geothermal reservoirs," *Journal of Earth Science*, vol. 26, no. 1, pp. 28–36, 2015.
- [48] F. Cappa, "Modelling fluid transfer and slip in a fault zone when integrating heterogeneous hydromechanical characteristics in its internal structure," *Geophysical Journal International*, vol. 178, no. 3, pp. 1357–1362, 2009.
- [49] Y. Zhang, M. B. Clennell, C. D. Piante, S. Ahmed, and J. Sarout, "Numerical modelling of fault reactivation in carbonate rocks under fluid depletion conditions – 2D generic models with a small isolated fault," *Journal of Structural Geology*, vol. 93, pp. 17–28, 2016.
- [50] F. Cappa, "Influence of hydromechanical heterogeneities of fault zones on earthquake ruptures," *Geophysical Journal International*, vol. 185, no. 2, pp. 1049–1058, 2011.
- [51] W. B. Fei, Q. Li, X. C. Wei, R. R. Song, M. Jing, and X. C. Li, "Interaction analysis for CO<sub>2</sub> geological storage and underground coal mining in Ordos Basin, China," *Engineering Geology*, vol. 196, pp. 194–209, 2015.
- [52] S. T. Nabavi, S. A. Alavi, S. Mohammadi, M. R. Ghassemi, and M. Frehner, "Analysis of transpression within contractional fault steps using finite-element method," *Journal of Structural Geology*, vol. 96, pp. 1–20, 2017.
- [53] A. P. Rinaldi, J. Rutqvist, and F. Cappa, "Geomechanical effects on CO<sub>2</sub> leakage through fault zones during large-scale underground injection," *International Journal of Greenhouse Gas Control*, vol. 20, pp. 117–131, 2014.
- [54] J. Angelier, "From orientation to magnitudes in paleostress determinations using fault slip data," *Journal of Structural Geology*, vol. 11, no. 1-2, pp. 37–50, 1989.
- [55] G. Ballas, H. Fossen, and R. Soliva, "Factors controlling permeability of cataclastic deformation bands and faults in porous sandstone reservoirs," *Journal of Structural Geology*, vol. 76, pp. 1–21, 2015.
- [56] M. Karimnezhad, H. Jalalifar, and M. Kamari, "Investigation of caprock integrity for CO<sub>2</sub> sequestration in an oil reservoir using a numerical method," *Journal of Natural Gas Science and Engineering*, vol. 21, pp. 1127–1137, 2014.
- [57] B. Ren, Y. Xu, S. Ren, X. Li, P. Guo, and X. Song, "Laboratory assessment and field pilot of near miscible CO<sub>2</sub> injection for IOR and storage in a tight oil reservoir of Shengli Oilfield China," in *SPE Enhanced Oil Recovery Conference*, pp. 1–11, Kuala Lumpur, Malaysia, 2011, Society of Petroleum Engineers.
- [58] T. C. Hanks, "b values and  $\omega^{-\gamma}$  seismic source models: implications for tectonic stress variations along active crustal fault zones and the estimation of high-frequency strong ground motion," *Journal of Geophysical Research*, vol. 84, no. B5, p. 2235, 1979.
- [59] H. Kanamori and D. L. Anderson, "Theoretical basis of some empirical relations in seismology," *Bulletin of the Seismological Society of America*, vol. 65, pp. 1073–1095, 1975.
- [60] P. Wriggers, *Computational Contact Mechanics*, Springer, Berlin, Heidelberg, 2006.
- [61] Z. Niu, Q. Li, and X. Wei, "Estimation of the surface uplift due to fluid injection into a reservoir with a clayey interbed," *Computers and Geotechnics*, vol. 87, pp. 198–211, 2017.
- [62] A. Mazzoldi, A. P. Rinaldi, A. Borgia, and J. Rutqvist, "Induced seismicity within geological carbon sequestration projects: maximum earthquake magnitude and leakage potential from undetected faults," *International Journal of Greenhouse Gas Control*, vol. 10, pp. 434–442, 2012.
- [63] R. Hillis, "Pore pressure/stress coupling and its implications for seismicity," *Exploration Geophysics*, vol. 31, no. 1-2, pp. 448–454, 2000.
- [64] A. P. Rinaldi, V. Vilarrasa, J. Rutqvist, and F. Cappa, "Fault reactivation during CO<sub>2</sub> sequestration: effects of well orientation on seismicity and leakage," *Greenhouse Gases: Science and Technology*, vol. 5, no. 5, pp. 645–656, 2015.
- [65] P. J. van Ruth, E. J. Nelson, and R. R. Hillis, "Fault reactivation potential during CO<sub>2</sub> injection in the Gippsland Basin, Australia," *Exploration Geophysics*, vol. 37, no. 1, pp. 50–59, 2006.
- [66] J. P. Verdon, J. M. Kendall, A. C. Horleston, and A. L. Stork, "Subsurface fluid injection and induced seismicity in Southeast Saskatchewan," *International Journal of Greenhouse Gas Control*, vol. 54, pp. 429–440, 2016.
- [67] S. A. Mathias, J. G. Gluyas, G. J. G. Martinez de Miguel, and S. A. Hosseini, "Role of partial miscibility on pressure buildup due to constant rate injection of CO<sub>2</sub> into closed and open brine aquifers," *Water Resources Research*, vol. 47, no. 12, 2011.
- [68] F. Cappa and J. Rutqvist, "Impact of CO<sub>2</sub> geological sequestration on the nucleation of earthquakes," *Geophysical Research Letters*, vol. 38, no. 17, article L17313, 2011.



**Hindawi**

Submit your manuscripts at  
[www.hindawi.com](http://www.hindawi.com)

